PMSat: Optimizing Passive Metasurface for Low Earth Orbit Satellite Communication

Hao Pan
Microsoft Research Asia
panhao@microsoft.com

Lili Qiu*
Microsoft Research Asia
UT Austin
liliqiu@microsoft.com

Bei Ouyang†
Microsoft Research Asia
happybei981101@gmail.com

Shicheng Zheng†
University of Science and Technology of China
sc7543@mail.ustc.edu.cn

Yongzhao Zhang†
Shanghai Jiao Tong University
zhangyongzhao@sjtu.edu.cn

Yi-Chao Chen†
Shanghai Jiao Tong University
yichao@sjtu.edu.cn

Guangtao Xue
Shanghai Jiao Tong University
gt_xue@sjtu.edu.cn

ABSTRACT

Low Earth Orbit (LEO) satellite communication is essential for wireless communication. While manufacturing and launching LEO satellites have become efficient and cost-effective, ground stations remain expensive due to complex designs for handling severe path losses and precise beam tracking. Hence, it is important to develop low cost and high-performance ground stations for widespread adoption of LEO satellite communication. Towards realizing this goal, we design a passive metasurface-enhanced LEO ground station system, named PMSat, combining metasurface's fine-grained beamforming capability with a small-size phased array's adaptive steering and focusing. For uplink, we jointly optimize the phase array codebook and uplink metasurface phase profile, and realize electronic steering by switching the codeword. We further jointly optimize the downlink metasurface phase profile to improve the focusing performance and enhance the received signal strength (RSS) over a wide range of incident angles. Our PMSat prototype consists of a single passive metasurface with 21×21 elements for uplink and 22×22 for downlink, along with 1×4 receiving and 1×4 transmitting phased array antennas. The effectiveness of our proposed PMSat is validated through extensive experiments, and results demonstrate that the optimized metasurface improves the SNR by 8.32 *dB* and 16.57 *dB* for uplink and downlink, respectively.

CCS CONCEPTS

• **Hardware → Wireless devices**; • **Networks → Wireless access points, base stations and infrastructure**.

KEYWORDS

LEO satellite communication; passive metasurface; phased array antennas

ACM Reference Format:
Hao Pan, Lili Qiu, Bei Ouyang, Shicheng Zheng, Yongzhao Zhang, Yi-Chao Chen, and Guangtao Xue. 2023. PMSat: Optimizing Passive Metasurface for Low Earth Orbit Satellite Communication. In *The 29th Annual International Conference on Mobile Computing and Networking (ACM MobiCom '23), October 2–6, 2023, Madrid, Spain.* ACM, New York, NY, USA, 15 pages. https://doi.org/10.1145/3570361.3613257

1 INTRODUCTION

Low Earth Orbit (LEO) satellite communication is promising to address the digital divide and improve worldwide connectivity. Recent advances in satellite technology have significantly reduced LEO satellite manufacture and launch costs [30]. However, the high cost of ground stations limits the widespread deployment of LEO satellite communication [35]. LEO networks typically utilizes millimeter-wave (mmWave) frequency to achieve high throughput, so the ground stations must address large mmWave signal path loss. To keep track of rapidly moving LEO satellites, the ground stations need accurate and fast beam tracking and steering to achieve good connectivity, which significantly increases complexity and cost of the transceiver device of ground stations.

*Lili Qiu is the corresponding author
†Bei Ouyang, Shicheng Zheng, and Yongzhao Zhang did this work as interns at Microsoft Research Asia and Yi-Chao Chen did this work as a visiting researcher at Microsoft Research Asia

ACM MobiCom '23, October 2–6, 2023, Madrid, Spain

ACM ISBN 978-1-4503-9990-6/23/10…$15.00
https://doi.org/10.1145/3570361.3613257

Parabolic antennas, commonly used in satellite communication networks, enhance received signal strength (RSS) through physical wavefront compensation but rely on bulky mechanical devices for steering direction adjustment. Alternatively, massive phased array antennas provide signal focusing and electronic beam steering without physical movement and achieve a compact form factor. Realizing high-resolution beam steering requires a large number of antennas and phase shifters, which incurs considerable costs especially for mmWave [25].

Metasurface technology enables flexible and accurate control over electromagnetic (EM) wavefronts, and presents a unique opportunity to enhance performance in wireless communication networks. Prior research has developed metasurfaces across various frequency bands (*e.g.*, Wi-Fi [7], mmWave [28], and cellular [13]) to achieve beam-splitting and improve RSS. Programmable metasurfaces can adapt to dynamic and unknown wireless channel and have been extensively studied, but they require programmable components like variable capacitors, diodes, additional microcontrollers and power supplies, which incur significant cost. In LEO networks, satellites move in pre-defined orbits, simplifying metasurface design. Therefore, our goal is to develop a low-cost, compact, and power-independent ground station leveraging passive metasurfaces.

Despite considerable work on metasurfaces, several significant challenges arise in realizing a practical passive metasurface for LEO applications. First, LEO satellite communication systems use separate frequency bands for uplink and downlink to ensure efficient and interference-free communication between ground stations and satellites [12]. Using a single metasurface for both uplink and downlink can reduce costs and save space, but it is challenging to avoid interference between the uplink and downlink. Second, during uplink communication, since the transmission antennas and passive metasurface remain stationary while LEO satellites continuously move, it is crucial for the outgoing signal from the metasurface to consistently steer towards the current satellite's position. However, a passive metasurface cannot be reconfigured after fabrication. Therefore, designing a stationary and passive metasurface capable of dynamically steering EM signals from transmission antennas towards moving LEO satellites is a demanding task. Third, during downlink communication, a constantly moving LEO satellite results in a continuously changing incident angle. The metasurface needs to re-direct the incoming signal from all possible incident angles towards the receiving antennas to enhance RSS.

In this paper, we propose a passive metasurface-enhanced LEO ground station system, called PMSat. We jointly optimize a passive metasurface and a small phased array to realize a cost-effective and high-performance transceiver antenna system for LEO. To address the above challenges, we begin by designing a transmissive metasurface unit cell (also called meta-atom) suitable for LEO scenarios. Metasurfaces manipulate EM wavefronts as each meta-atom introduces phase shifts to incoming signals with minimal power loss. Our designed meta-atom must satisfy high transmittance (*e.g.*, above 90%) and a 360° phase modulation range for effective control and adaptation of outgoing EM waves. Moreover, the meta-atom should support dual frequency bands and wide incident angles in LEO scenarios. To support dual bands using a single metasurface, we use a "metal-substrate-metal" sandwich structure as meta-atoms for both uplink and downlink. We then arrange the two patterns as a basic structure, positioning the downlink pattern in the center and the uplink pattern at the corners. We optimize hyperparameters to determine the optimal geometric parameters of the basic structure to achieve *high transmittance*, 360° *phase shift coverage*, *wide-incident-angle support*, and *minimized interference* for both uplink and downlink.

Furthermore, in order to realize passive metasurfaces with dynamic focusing and steering capabilities, we propose a unique integration of the passive metasurface with a small phased array (*e.g.*, 1×4 antennas). This distinctive combination enables us to simultaneously leverage the powerful wavefront manipulation capability in metasurfaces to implement fine-grained beamforming and exploit software-based phased array antennas to dynamically beam steering by switching codewords. Specifically, in the uplink, our optimized metasurface steers EM wave emitted from the phased array using various codewords toward target satellites. In the downlink, our metasurface enhances the RSS by focusing the EM waves from target satellites onto the receiving phased array antennas. An important design issue is how to optimize the phase map of the passive metasurface and codewords of the phased array in the uplink and downlink. To address this problem, we present a channel model of the phased array and metasurface, including the near-field channel response between each antenna and each metasurface element. Then, we cast the joint-design of the phased array codebook (*i.e.*, weights of the feeding source for each antenna) and the metasurface's phase compensation map (*i.e.*, phase shift of each metasurface element) as optimization problems. We employ a gradient descent based algorithm to obtain optimized configurations. For the uplink, our optimization provides phased array codewords for each desired outgoing angle and a fixed metasurface phase map. For the downlink, our optimization yields a metasurface phase map that focuses incoming signal onto receiving antennas across a wide range of incidence angles. Note that our proposed system is flexible enough to support electronic beam steering towards multiple satellites and focus signals from multiple satellites. The ability to communicate with multiple satellites is appealing, as it can eliminate service disruption

during hard handovers (*i.e.*, breaking the connection with the previous satellite before connecting with the new satellite).

To validate the proposed PMSat, we fabricate our optimized passive metasurface using PCB processing technology, comprising 21×21 uplink elements and 22×22 downlink elements. We also implement a transceiver antenna prototype board containing two 1×4 antenna arrays, one for the uplink (*i.e.*, $30GHz$) and another downlink (*i.e.*, $20GHz$). Our system weighs a total of 132g, including the metasurface ($80.25g$), the transceiver antenna board ($19.81\ g$), and a 3D-printed bracket ($32.36\ g$) that secures the metasurface and phased array. We conduct evaluations using theoretical analysis, a high-fidelity EM simulator (HFSS), and real-world testbed experiments. Experimental results in both an anechoic chamber and outdoor environments validate the HFSS simulation and demonstrate the feasibility and effectiveness of our proposed system. Our optimized metasurface provides an average gain of $16.57\ dB$ in the downlink and $8.32\ dB$ in the uplink over a 1×4 phased array alone.

Our contributions can be summarized as follows.

- Our work, named PMSat, develops a joint optimization for passive metasurface and small phased-array antennas. This unique combination leverages metasurfaces' fine-grained beam steering and a phased array's dynamic adaptation by switching codewords. It presents an attractive solution to a low-cost ground station.
- We design a single metasurface to simultaneously support uplink and downlink. Utilizing a hyperparameter tuning algorithm, we efficiently search for a near-optimal structure of meta-atom to meet LEO scenario requirements: high transmission (*e.g.*, over 90%), 360° phase-shift coverage, wide frequency bands (*e.g.*, $29 - 30\ GHz$ for downlink and $19 - 20\ GHz$ for downlink), and wide incidence angle (*e.g.*, $-40° \sim 40°$). While this paper focuses on LEO scenarios, our methodology and metasurface design can be applied to other frequency bands and wireless networks.
- We implement a prototype and conduct thorough evaluation to demonstrate the effectiveness of the PMSat. Furthermore, we show that our system is flexible enough to direct beams and focus signals towards and from multiple satellites. We release our code at https://github.com/microsoft/PMSat.

2 RELATED WORK

2.1 LEO Satellite Communication

LEO satellite communication offers many benefits, such as global coverage and low latency. However, it faces several significant challenges. First, the limited power and low signal-to-noise ratio (SNR) of the satellite-to-Earth link limit data rates. Next, the rapid movement of LEO satellites necessitates ground stations to track satellites, increasing their size, complexity, and cost. Additionally, each satellite has only a small coverage area and requires handovers; if handoff is too frequent or insufficient, the user will experience poor performance and even service disruption.

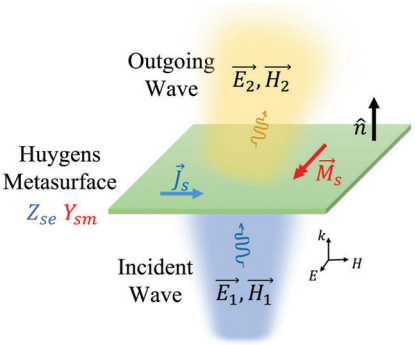

Figure 1: The schematic of Schelkunoff's equivalence principle illustrates how a Huygens metasurface can transform an incident EM wave $(\overrightarrow{E_1}, \overrightarrow{H_1})$ into an outgoing EM wave $(\overrightarrow{E_2}, \overrightarrow{H_2})$

Traditionally, satellite ground stations often employ a parabolic antenna, which is bulky, expensive, and has difficulty in tracking fast-moving satellites. As an alternative, massive phased array antennas electronically steer signals without movement. However, this requires a large number of antennas in order to realize accurate tracking, which increases the cost. Recently, there is an increased interest in improving ground station transceivers for LEO satellite systems. SatNOGS [29] develops an open-source project for constructing a basic ground station with a parabolic dish antenna, expanding coverage by accessing other stations worldwide. This only costs $\$300 - \$500$, making personal use of LEO possible. However, the basic platform struggles to decode low-SNR signals and extra hardware is needed to eliminate noise. Quasar [31] proposes using multiple low-cost stations to recover signals but is limited to broadcast data in specialized scenarios.

Inspired by prior work and challenges in LEO networks, our research advances the state of the art by employing a passive metasurface and miniature-scale phased array to focus and steer signals in both downlink and uplink.

2.2 Huygens Metasurface

Metasurfaces, also known as metamaterials or smart surfaces, are a type of artificial sub-wavelength structure with negligible thickness. Among them, Huygens Metasurfaces (HMS) can respond to electric and magnetic fields by forming virtual dipoles. The HMS is particularly attractive due to its ability to provide full control over amplitude and phase of the transmitted and reflected waves, enabling efficient wavefront shaping. This ability stems from Schelkunoff's equivalence principle, a generalization of Huygens' principle. As shown

in Fig 1, a given incident EM wave $(\overrightarrow{E_1}, \overrightarrow{H_1})$ can be converted to a desired wave $(\overrightarrow{E_2}, \overrightarrow{H_2})$ by inducing orthogonal electric and magnetic currents $(\overrightarrow{J}, \overrightarrow{M})$ to the metasurface, where $\overrightarrow{J} = \hat{n} \times (\overrightarrow{H_2} - \overrightarrow{H_1})$ and $\overrightarrow{M} = -\hat{n} \times (\overrightarrow{E_2} - \overrightarrow{E_1})$. Furthermore, the electric and magnetic currents are directly determined by the surface impedance (Z_{se}), surface admittance (Y_{sm}) and the average tangential incident fields $(\overrightarrow{E_t}, \overrightarrow{H_t})$. Therefore, the aforementioned equation can be expressed as follows: $\overrightarrow{E_t} = Z_{se} \cdot [\hat{n} \times (\overrightarrow{H_2} - \overrightarrow{H_1})]$, $\overrightarrow{H_t} = Y_{sm} \cdot [-\hat{n} \times (\overrightarrow{E_2} - \overrightarrow{E_1})]$. Therefore, once the incident and desired EM fields are defined, the surface impedance and admittance of the desired HMS can be calculated. Researchers typically design HMS geometries, structures, and materials to achieve these values. The next part of this section provides a brief overview of metasurfaces in wireless communication.

Programmable metasurface. Programmable metasurfaces are capable of controlling EM waves in real-time by utilizing active elements, such as positive intrinsic-negative (PIN) diodes [16], varactor diodes [33], phase changing materials [15], liquid crystals [36], and RF switches [17]. Tan *et al.*employed a reflect-array to control the reflected wave phase shift of each patch using a RF switch [32]. However, their responsiveness is limited as they need to be synchronized with transmitters. Venkat *et al.*developed a smart surface to realize beamforming, called *RFocus* [3], which includes thousands of RF switches to control whether Wi-Fi signals are reflected or passed through. Zelaya *et al.*developed a large array of vanilla amplifiers (LAVA) to extend indoor wireless coverage [38], where each LAVA element has a power sensor to detect transmission and control connected amplifiers. mmWall [10] addressed the problem of mmWave line-of-sight blockages by using a reconfigurable meta-atom with two resonant rings to relay and re-direct beams. Wall-E [9], another reconfigurable metasurface, is designed as a dual-band solution to the beam alignment problem under complex environments. Programmable metasurfaces often require an additional controller connected to each component through wires, increasing system complexity, deployment difficulty, and power supply needs. Programmable elements in high-frequency bands (*e.g.*, mmWave) can be costly and make the metasurface's cost comparable to a massive phased array of the same size.

Passive metasurfaces. Metallic reflectors have been studied for extending wireless coverage in datacenter [40], indoor [19], and outdoor [26] scenarios. Unlike metallic reflective surfaces, passive metasurfaces are composed of periodic meta-atoms with specific patterns that can be designed for either transmission or reflection. Furthermore, passive metasurfaces can be configured with unique phase compensation profiles to manipulate wavefront for various applications. Qian *et al.*developed MilliMirror, a 3D printed passive metasurface, to steer the reflected signals and address mmWave blockage issues [28]. Nevertheless, these designs behave like mirrors reflecting mmWave signals towards NLOS directions, and cannot support dynamic steering, which is not appropriate for LEO satellite communication. Lima *et al.*proposed a simple mechanical beam steering metasurface concept for $Ka-$band satellite communication [21], but cannot realize dynamic beam steering using only a passive metasurface. [22, 37] consider applying metasurface to phased array to reduce the cost.

To conclude, passive metasurfaces used at ground stations for LEO communication need to achieve fine-grained dynamic steering and focusing for both uplink and downlink. Thus, the designed meta-atom should support a 360° phase shift range and high transmission efficiency in dual frequency bands and wide incident angles. In the following section, we will explore the detailed techniques for optimizing passive metasurfaces at both microscopic and macroscopic levels to meet the requirements for LEO applications.

3 DUAL-BAND PASSIVE METASURFACE DESIGN FOR LEO

Metasurfaces are structured surfaces designed to manipulate EM wavefronts by introducing a precise phase shift on each metasurface cell. The metasurface design consists of two parts: macroscopic design and microscopic design. Our metasurface microscopic design selects a meta-atom that can support 360° phase shift coverage with high transmittance. This requires careful selection of substrate material, structure, and geometric patterning. Our macroscopic design determines the phase of each metasurface cell, also called a phase compensation map configuration. We implement the optimized phase map profile configuration by placing meta-atoms at appropriate locations in the metasurface. In this section, we first present the microscopic design for LEO, and then describe the macroscopic design for uplink and downlink phase map profiles to achieve dynamic fine-grained focusing and steering using a combination of a passive metasurface and small phase array.

3.1 Microscopic Design: Meta-atom

In the LEO scenario, our meta-atom design must support *dual-widebands*, 360° *phase shift range*, and *wide incident angles*. Specifically, a single metasurface should support both uplink and downlink communication, with each meta-atom achieving high transmittance and $0 \sim 360°$ phase shift control. As LEO networks use widebands for increased link capacity[1],

[1]Amazon's Kuiper LEO satellites use $17.7 \sim 18.6GHz$ and $18.8 \sim 20.2GHz$ for the downlink (satellite-to-Earth) and $27.5 \sim 30.0GHz$ for the uplink (Earth-to-satellite) [11].

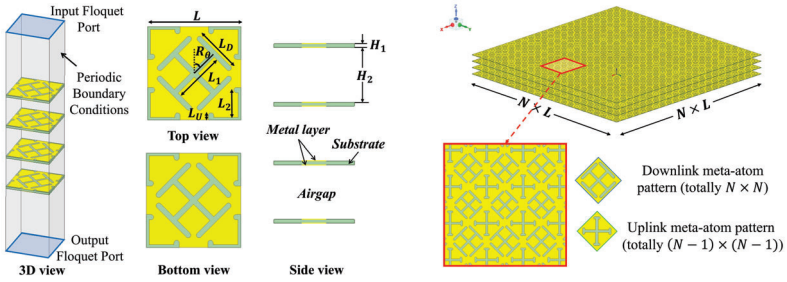

(a) Microsopic: structural geometry of the proposed meta-atom suitable for LEO

(b) Macrosopic: arrangement of meta-atoms to form metasurface

Figure 2: (a) Optimized meta-atom features a multi-layer structure with a yellow metal layer and a green substrate layer. (b) Metasurface is composed of hundreds of meta-atoms for EM wavefront manipulation

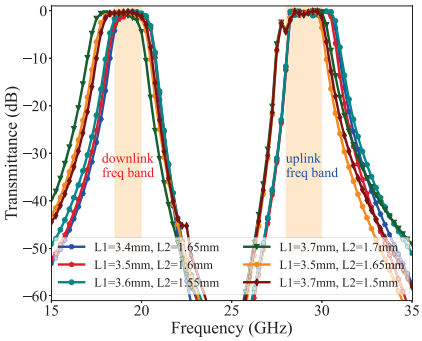

Figure 3: Examples of frequency response of transmission amplitude for different values of pattern parameters

the meta-atom should maintain similar phase shift and transmission capabilities across the entire band used by the uplink and downlink. Since satellites move constantly, the design should ensure incident waves with various angles achieve high transmittance and phase control ability. The fast satellite movement induces Doppler shift. LEO satellite networks like Starlink estimate Doppler shifts by tracking the target satellite's location and velocity and compensate for the Doppler shift. For example, with a satellite orbit 370 miles above Earth and a carrier frequency at $20GHz$, the maximum Doppler shift is $0.0002GHz$ [1]. This is within the meta-atom operating frequency range and allows proper signal reception. After receiving the signal, the Doppler shift can be compensated.

3.1.1 Meta-atom geometry. Several existing works design HMSs with specific copper patterns overlaid on a substrate [8]. The meta-atoms in these HMSs have electric dipole elements that induce electric currents, and these currents can also induce orthogonal magnetic currents, ultimately exciting electromagnetic resonance and achieving efficient transmission or reflection [14]. In this paper, we design specific geometries of copper patterns on the dielectric substrate and pack them closely to implement a single meta-atom for both the downlink and uplink.

Downlink pattern: We design a Jerusalem cross-shaped element (as seen in the center of Fig. 2(b)) for the downlink. We choose this pattern because cross-slot structures provide relatively complete phase control while maintaining low-loss transmission [4, 39]. The phase regulating parameters of the downlink are L_1 and L_D, and they are tuned together and linked by the relationship $L_D = \frac{L_1}{k}$, where k is a constant related to the decoupling performance. This means that we can obtain different phase responses of the meta-atom by applying different L_1 parameters.

Uplink pattern: We design another Jerusalem cross element (see the four corners of Fig. 2(b)) for the uplink. Note that the metasurface is composed of periodically arranged meta-atoms, so these four corners in each meta-atom maintain cross-slot structure (see Fig. 2(b)). Similarly, L_2 and L_U are the phase regulating parameters for the uplink. To save space and avoid overlapping with the downlink patterns, we fix L_U to be a small constant ($0.25\ mm$) and only adjust L_2 to realize phase modulation.

Decoupling angle: Coupling occurs between adjacent patterns when placed close together. For example, interaction between slots with lengths L_D and L_2 creates a new capacitance, altering the meta-atom's surface impedance. To reduce interference from coupling, a decoupling parameter, R_θ, adjusts the relative position of downlink and uplink patterns.

Multiple layers: To enhance the transmittance and phase shift coverage for both the downlink and uplink, we employ a multi-layer structure. As illustrated in Fig. 2(c), layers are separated by air gaps with a height of H_2, and all layers share the same geometric design.

Since we design a transmissive metasurface, we use the transmittance parameter $S21$ to derive the frequency response of meta-atom design. Specifically, $|S21|$ and $\angle S21$ represent the transmittance and phase response of the metasurface, respectively. We build a meta-atom model in the Ansys HFSS simulator [2] with Floquet port excitation mode, as shown in Figure 2(a). An example of our meta-atom's frequency response of transmission amplitude is shown in Fig.3, as we vary the downlink and uplink phase regulating parameters (*i.e.*, L_1 and L_2). The other structure parameters are set to their default values: $M = 2$, $L = 5.3mm$, $k = 3$, $L_U = 0.1mm$, $R_\theta = 0°$, $H_2 = 2.5mm$, the permittivity of substrate (ε) is 2.2. Our results show that our closely packed meta-atom consisting of downlink and uplink patterns can support both frequency bands with over 90% energy transmission.

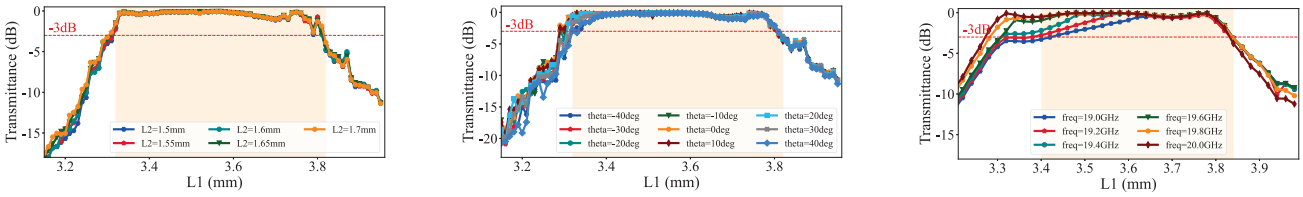

(a) Transmittance at different L_1 parameters with $\theta_i = 0°$ and $f_{down} = 20GHz$

(c) Transmittance at different incident angles with $L_2 = 1.6mm$ and $f_{down} = 20GHz$

(e) Transmittance at different frequency points with $L_2 = 1.6mm$ and $\theta_i = 0°$

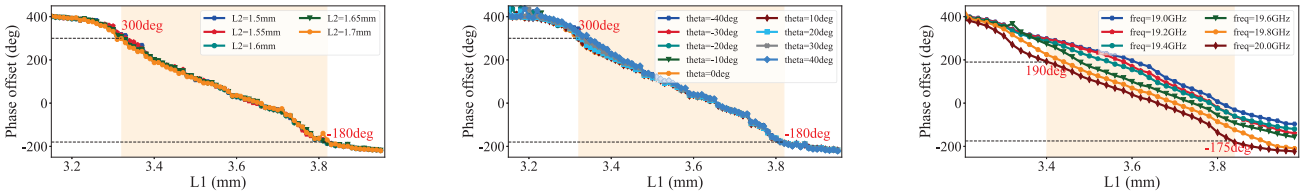

(b) Phase offset at different L_1 parameters with $\theta_i = 0°$ and $f_{down} = 20GHz$

(d) Phase offset at different incident angles with $L_2 = 1.6mm$ and $f_{down} = 20GHz$

(f) Phase offset at different frequency points with $L_2 = 1.6mm$ and $\theta_i = 0°$

Figure 4: Transmission amplitude and phase responses of the optimal unit cell at downlink frequency bands

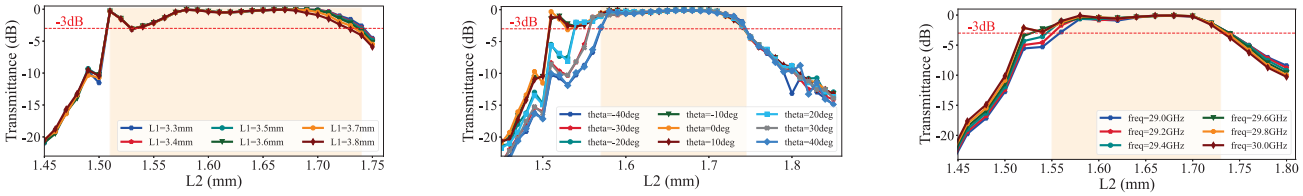

(a) Transmittanc under different L_1 paras with $\theta_i = 0°$ and $f_{up} = 30GHz$

(c) Transmittance under different incident angles with $L_2 = 3.6mm$ and $f_{up} = 30GHz$

(e) Transmittance at different frequency points with $L_1 = 3.6mm$ and $\theta_i = 0°$

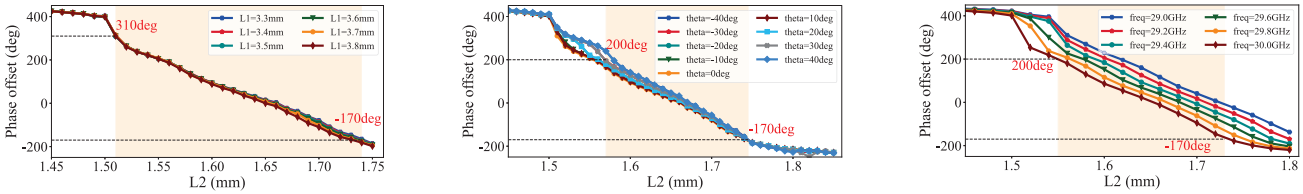

(b) Phase offset under different L_1 paras with $\theta_i = 0°$ and $f_{up} = 30GHz$

(d) Phase offset under different incident angles with $L_2 = 3.6mm$ and $f_{up} = 30GHz$

(f) Phase offset at different frequency points with $L_1 = 3.6mm$ and $\theta_i = 0°$

Figure 5: Transmission amplitude and phase responses of the optimal unit cell at uplink frequency bands

3.1.2 Structure parameter optimization. Among all parameters in the meta-atom design, L_1 and L_2 are the variables that regulate phase shifts of incident waves in the downlink and uplink. L_1 ranges from $3.0mm$ to $4.0mm$. We let $\vec{L_1}$ denote the set of L_1 values, *i.e.*, the phase shift vector for downlink. L_2 ranges from $1.4mm$ to $1.8mm$. We let $\vec{L_2}$ denote the set of L_2 values, *i.e.*, the phase shift vector for uplink . The permittivity of substrate is set to 2.2. We optimize the remaining hyperparameters associated with the meta-atoms for both the downlink and uplink to achieve the following three key requirements: (i) 360° of phase shift coverage, (ii) a wide range of incident angles (*i.e.*, $-40° \sim 40°$), and (iii) a wide bandwidth (*i.e.*, $1 \sim 1.5GHz$).

We define a set of hyperparameters $\vec{SP}$ to optimize. This set includes all candidate structure hyperparameters: the number of layers (M), airgap height (H_2), unit pattern length (L), downlink decoupling parameters k (*i.e.*, $k = \frac{L_1}{L_D}$), R_θ, and uplink decoupling parameter L_U. We also define our optimization objective function as follow:

$$\arg\max_{\vec{SP}} \left(\sum_{\vec{\theta_i}} \sum_{\vec{f_{down}}} \sum_{\vec{L_2}} F_d(\vec{L_1}) + \sum_{\vec{\theta_i}} \sum_{\vec{f_{up}}} \sum_{\vec{L_1}} F_u(\vec{L_2}) \right),$$

$$F_d(\vec{L_1}) = tanh(max(\angle S21(\vec{L_1})) - min(\angle S21(\vec{L_1})) - 360°),$$

$$F_u(\vec{L_2}) = tanh(max(\angle S21(\vec{L_2})) - min(\angle S21(\vec{L_2})) - 360°)$$

where $tanh()$ is the hyperbolic tangent function, $\vec{\theta_i}$ is a set of incident angles towards meta-atom with θ_i ranging from $-40°$ to $40°$, $\vec{f_{down}}$ is a set of frequencies in the downlink ranging from $19GHz$ to $20GHz$, and $\vec{f_{up}}$ is the uplink frequency band ranging from $29GHz$ to $30GHz$. $\vec{L_1} = \omega : |S21|_{dB}(L_1) > -3$, denotes the set of L_1 that satisfies attenuation within $3dB$ in the downlink. $\vec{L_2} = \omega : |S21|_{dB}(L_2) > -3$, denotes the set of L_2 that satisfies attenuation within $3dB$ in the uplink. Note that the $S21$ parameters of a meta-atom are calculated by HFSS based on $\vec{SP}$, $\vec{L_1}$, and $\vec{L_2}$. Note that we use $tanh()$ in the optimization objective because our goal is to ensure $max(\angle S21(L_1)) - min(\angle S21(L_1))$ is close to 360^o and further increasing their difference beyond 360^o is not useful due to phase wrap-around. We sum up $F_d(L_1)$ across all angles, all frequencies, and all values of L_2 to achieve wide angle, wide band, and decoupling from the uplink. The same thing is done for $F_u(L_2)$.

Our goal is to determine the optimal set of structure parameters, denoted by $\vec{SP} = \{M, H_1, H_2, L, k, R_\theta\}$ that maximizes the dual-band meta-atom performance. To tackle this combinatorial optimization problem, which has discrete solutions, we employ a Tree-structured Parzen Estimator [5], a well-known Bayesian optimization algorithm, to optimize the parameters of the meta-atom. The final structure hyperparameters of the meta-atom satisfying the LEO SATCOM scenarios are as follow: $M = 4$, $H_1 = 0.254mm$, $H_2 = 3.6mm$, $L = 5.3mm$, $k = 1.5$, *and* $R_\theta = 45°$.

Fig. 4 and 5 show the performance of our dual-band meta-atom. By varying L_1 from $3.32mm$ to $3.81mm$, we obtain $360°$ phase shift coverage with high transmittance at $20GHz$, as shown in Fig. 4(a) and 4(b). Its phase shift capability is almost independent of L_2, which indicates a good decoupling effect. Our meta-atom design also proves to be insensitive to the wide incident angles from $-40°$ to $40°$ in the downlink, as shown in Fig. 4(c) and 4(d). The proposed meta-atom can also work well across different frequencies. The results are shown in Fig. 4(e) and 4(f). Note that the phase offset versus L_2 curves change across different frequencies, but they still share a similar slope. The wavefront is not affected by changing the constant phase of all elements in the metasurface, as only the phase difference between the elements is significant. Therefore, our meta-atom achieves almost the same phase shift capability with high transmittance across the entire downlink frequency band. As for the performance in the uplink, Fig. 5(a) - 5(f) also validate that our meta-atom can support various incident angles and wide bands with $360°$ phase shift coverage and high transmittance.

After the microscopic design is complete, we can use our macroscopic phase profile design in Section 3.2 and 3.3 to determine the phase offsets in both the uplink and downlink

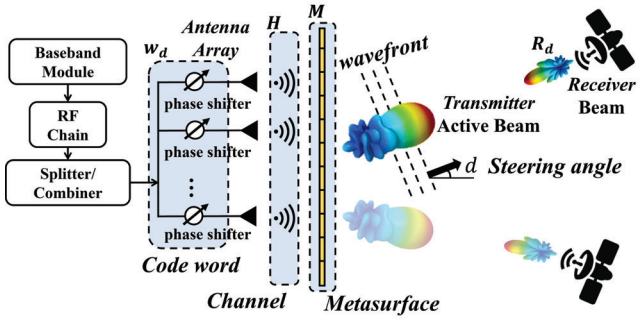

Figure 6: Working principle of electronic steering through phased array antennas and metasurface

of each meta-atom. To do this, we map the desired phase offset of each meta-atom to L_1 and L_2 using the curves in Fig 4(b) and 5(a). Then, we build a metasurface consisting of periodically arranged meta-atoms to realize the desired control of wavefront and radiation patterns. Our metasurface has $N \times N$ elements for downlink wavefront manipulation and $(N-1) \times (N-1)$ elements for uplink, as shown in Fig. 2(b).

3.2 Macroscopic Design for Uplink

Our goal for the uplink is to design a metasurface that directs the EM wave from the ground station towards the satellite's current position. Since we use a passive metasurface, we cannot change its phase delay profile after fabrication. We exploit the dynamic adaptation of a phased array to generate different wavefronts and leverage the passive metasurface to sharpen its outgoing beam. In order to achieve beam steering using a passive metasurface and a small antenna array, we formulate an optimization problem to determine the optimal metasurface phase profile and phased array codebook.

3.2.1 Steering with metasurface and phased array. Our goal is to shape the EM waves emitted from the phased array in a specific direction as they pass through the metasurface. Fig. 6 shows the design principle of our system. Below we formulate the optimization problem.

Codeword of phased array: For a given steering direction d, the EM waves are first radiated from the phased array with a codeword represented by $\vec{w_d}$, where each element is a complex number representing each antenna's feed signal. These EM waves then pass through the channel C between the phased array and metasurface.

Channel from phased array to metasurface: We define the channel matrix $\mathbf{H}$ between the antenna array and metasurface, where each element $H_{i,j}$ determines the complex channel response from the i-th antenna to the j-th metasurface unit, where $H_{i,j} = A_{i,j}e^{\theta_{i,j}}$, $A_{i,j}$ is the decay term, and $\theta_{i,j}$ is the phase delay term. For $A_{i,j}$, we use a common free-space path loss for fading information [27]: $A_{i,j} = \frac{\lambda}{4\pi d_{i,j}}$, where $d_{i,j}$ is the distance between the i-th antenna and j-th metasurface

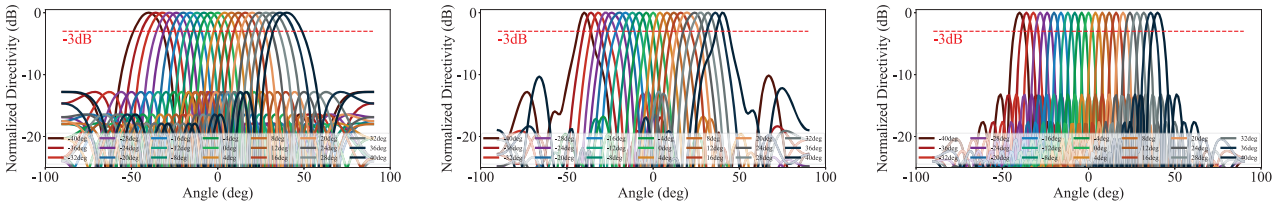

(a) 1 × 8 line PA with half wavelength spacing (b) 1×8 PA and metasurface with 21×21 elements (c) 1 × 21 PA with half wavelength spacing

Figure 7: Benefit of combining a passive metasurface and phased array antennas, showcasing fewer required antennas and enhanced directionality. These results depict the normalized beam patterns for different outgoing azimuth angles

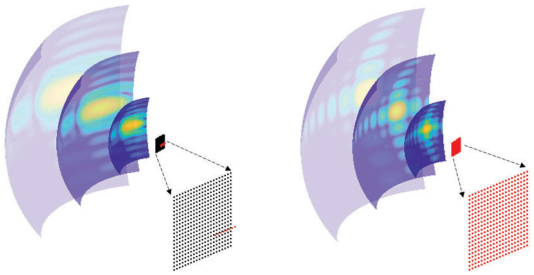

(a) 1 × 8 PA + 21 × 21 metasurface (b) 21 × 21 PA

Figure 8: Comparison of 3D beam propagation between (a) our design and (b) a same-size phased array, with red points for antennas and black points for metasurface

unit, and λ is the wavelength. We calculate the phase delay term as $\theta_{i,j} = \frac{2\pi d_{i,j}}{\lambda}$.

Channel of metasurface: A metasurface will change the incident EM waves through its own channel response: $M_j = A'_j e^{\theta'_j}$, where A'_j is the transmittance and θ'_j is the phase shift. The total channel matrix of the metasurface is $\mathbf{M}$, where $\mathbf{M}_{jj}$ defines the channel response of the j-th metasurface cell.

Outgoing wavefront: The outgoing wavefront from the metasurface *i.e.*, $\mathbf{MH}\vec{w}_d$, should be perpendicular to the EM wave propagation direction to allow the wave to move towards the satellites. Our goal is to determine the metasurface configuration (*i.e.*, $\mathbf{M}$) and codeword of phased array antennas (*i.e.*, $\vec{w}_d$) to maximize signal strength, $\vec{R}_d\mathbf{MH}\vec{w}_d$, along the desired steering direction (*i.e.*, d), where $\vec{R}_d$ is the steering vector.

Final optimization problem: Our system should steer the beam towards the LEO satellite in a range of angles as outlined in [6]. Specifically, we consider k (equal to 81) desired steering directions, denoted as $\vec{d} = [-40°, -39°, ..., 40°]$.

We introduce the received signal matrix, denoted as $\mathbf{S} = \sum_{d=-40°}^{d=40°} \vec{R}_d\mathbf{MH}\vec{w}_d$, which includes all desired steering directions. Through matrix manipulation, we express $\mathbf{T}$ in terms of the following constituent matrices: $\mathbf{T} = \mathbf{RMHW}$. $\mathbf{R}$ is an $k \times L$ matrix, where each row corresponds to a given direction d, and each column corresponds to the receive steering direction vector R_d. $\mathbf{M}$ is a $L \times L$ matrix, where L is the number of metasurface elements. The matrix $\mathbf{H}$ is of size $L \times N$, and represents the channel from the phased array (with N antennas) to the metasurface. $\mathbf{W}$ is a $N \times k$ codebook. In the above matrix, the steering matrix $\mathbf{R}$ is known in advance. The metasurface size, phased array size, and their relative positions, and channel $\mathbf{H}$ are also known. Our goal is to optimize the metasurface configuration $\mathbf{M}$ and phased array antenna codebook $\mathbf{W}$ that maximize the power of outgoing signal across a wide range of angles for given $\mathbf{R}$ and $\mathbf{H}$. Let $\mathbf{P}$ denote the power of the outgoing signal. We have $\mathbf{P} = |\mathbf{S}|^2$, so our problem can be formulated as follows:

$$\max_{\mathbf{M},\mathbf{W}} \quad tr(\mathbf{P}) - var(diag(\mathbf{P})) - ||sum(\mathbf{P}) - tr(\mathbf{P})||_F \qquad (1)$$

$$s.t. \begin{cases} |w_i| = 1, & (i = 1, 2, ..., N) \\ |\mathbf{M}_{j,j}| = 1, & (j = 1, 2, ..., L) \end{cases}$$

where $tr(\mathbf{P})$ denotes the trace of $\mathbf{P}$, $var(diag(\mathbf{P})$ denotes the variance of the diagonal elements in $\mathbf{P}$, and $(||sum(P)-tr(P)||$ represents the Frobenius norm (*i.e.*, the square root) of the sum of the absolute squares of all elements in $\mathbf{P}$ except the diagonal elements. The first term maximizes the power in the desired directions, the second term minimizes the variance of steering performance across different directions, and the third term minimizes the sidelobe. Our goal is to search M and W that maximize the objective. Due to cost constraints, commercial phased array antennas typically only utilize digital phase shifters to achieve phase delay, rather than including an amplifier for each individual antenna. Therefore, we assume $|w_i| = 1$, which limits each antenna to only adjust phase delay. We also assume the metasurface units have ideal transmittance by fixing $|\mathbf{M}_{j,j}| = 1$.

We utilize Adam [20], a stochastic gradient descent algorithm, to solve this problem. To ensure the constraints are satisfied, we normalize the current values of $\mathbf{M}$ after each iteration of gradient descent. The learning rate is set to 0.05, and the exponential decay rates for the first and second moment estimates are set to 0.9 and 0.999, respectively.

Comparison with massive phased array To demonstrate the effectiveness of our design, we develop an adaptive steering system using a 21 × 21 passive metasurface and a 1 × 8 small linear phased array. Our results in Fig. 7(a) and Fig. 7(b) show that our design offers adaptive beam steering and significantly

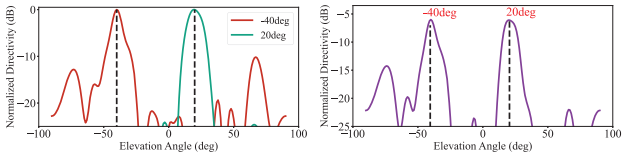

(a) Left: Radiation patterns for two steering angles: −40° and 20°. Right: A combining code word enabling steering at two angles

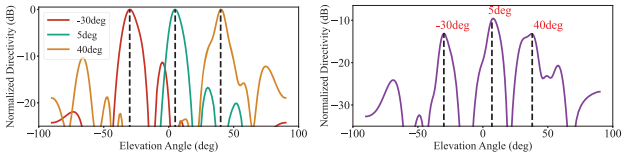

(b) Left: Radiation patterns for three steering angles: −30°, 5°, and 40°. Right: A combining code word enabling steering at three angles

Figure 9: Examples of PMSat supporting multiple beam steering directions simultaneously

out-performs a 1×8 phased array. Moreover, our system achieves comparable directionality to a 1×21 phased array in the azimuth dimension, as shown in Fig. 7(c). However, due to the 2D design of our metasurface, our design can provide directionality not just in the azimuth dimension, but also in the elevation dimension. As shown in Figs. 8(a) and 8(b), the EM waves coming from the metasurface indeed focus in both azimuth and elevation dimensions with strong directionality, and perform similarly to a 21×21 rectangular phased array but at a much reduced cost.

3.2.2 Supporting multiple beam steering. So far, we consider communicating with a single moving satellite. In practice, it is beneficial for a ground station to communicate with multiple satellites simultaneously to avoid disruption and provide smooth user experience when one satellite moves away or its signal is obstructed.

To support multi-beam steering, we let the ground station communicate with N satellites within its view, where the directions of these satellites correspond to $D = \{d_1, d_2, ..., d_N\}$. As described in Sec. 3.2.1, we can determine the optimal metasurface $\mathbf{M}$ and codewords that allow us to steer each of the desired angles separately. To support the steering of multiple beams, we weigh these codewords, sum them up, and then normalize, which yields $\vec{w} = \frac{1}{N}\sum_{d\in D} \vec{w}_d e^{j\theta_d}$. The term $e^{j\theta_d}$ introduces phase delays to each codeword w_d to maximize the power of the outgoing signals, while the $\frac{1}{N}$ term ensures that the total transmission power does not exceed 1. It is important to note that multiplying the phase compensation term $e^{j\theta_d}$ in each weight of the codeword has no impact on the beamforming direction. To determine the phase compensation term that supports multiple beams, we formulate the following optimization problem: $\arg\max_{\theta_a} \vec{w}^T \vec{w}$, where T means the Hermitian transpose [23].

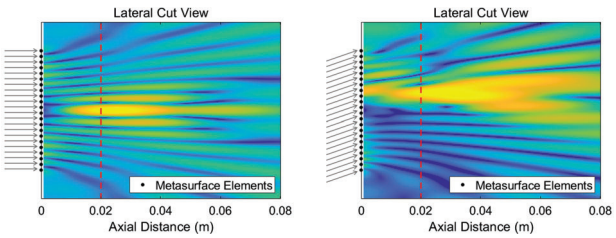

(a) Incident angle is 0° (b) Incident angle is 20°

Figure 10: Radiation fields of incoming satellite signals with varying angles demonstrate the exceptional focusing capabilities of our designed metasurface. Gray lines mean the incident EM waves, black points mean the metasurface unit, red dished line means the focal range

Fig. 9 shows our multi-beam steering performance using simulation. The left graph shows the three beam patterns associated with the three distinct codewords; the right figure shows our optimized single codeword generates multiple beams towards the three satellites simultaneously. When the power of the RF chain is increased to three times, each of the multi-beams is similar to the single-beam.

3.3 Macroscopic Design for Downlink

In our downlink design, our objective is to enhance RSS from the LEO satellites across a wide range of incident angles.

Different from the uplink, in the downlink we do not need to add phase shifters to beamform the receiving signals and can rely on the metasurface to focus energy. We denote the satellite transmission beam vector as $\vec{T_d}$ for a specific direction, that is also equivalent to the normalized wavefront vector of the plane wave that reaches the metasurface. The metasurface modulates the incident EM waves through a channel function, denoted as $\mathbf{M}$. The antenna array receiving the EM waves through the channel, denoted as $\mathbf{H}$. Antennas in the array then combines all received signals and produce the final output signal, $\mathbf{WHM}\vec{T_d}$, where $\mathbf{W}$ is a $1 \times N$ matrix and all elements are set to 1. Our goal is to maximize the received signal strength from the antenna array in the incident direction. We can model the receive signal in the downlink from all incident angles as a matrix: $\mathbf{S} = \mathbf{WHMT}$. We maximize the overall received signal power, *i.e.*, $P = |S|^2$, in the downlink by searching W and M that optimize the following objective:

$$\max_{\mathbf{M}} \quad sum(P) \qquad (2)$$
$$s.t. |\mathbf{M}_{j,j}| = 1, \quad (j = 1, 2, ..., L)$$

where $sum(S^2)$ represents the sum of power received by the antenna array. We also assume the metasurface units have ideal transmittance by fixing $|\mathbf{M}_{j,j}| = 1$. Unlike in the uplink case, we do not have $|w_i| = 1$ since the downlink receiver can combine the signals from different antennas using different

(a) Overview of the fabricated PMSat prototype (b) Top and bottom view of fabricated metasurface (c) Top and bottom view of fabricated transceiver antenna array

Figure 11: Photograph of the fabricated prototype of our proposed PMSat

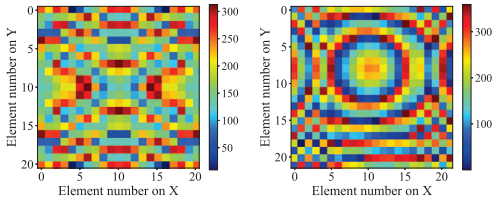

(a) Uplink phase profile (b) Downlink phase profile

Figure 12: Optimized compensating phase distributions of our designed metasurface

scaling factors, which differ in both phases and magnitude whereas the transmitter in the uplink can only change the phases of the outgoing signals from different antennas but not the amplitudes since a power splitter in the uplink phased array antennas distributes equal power to each antenna.

Fig. 10 show examples of two different incident angles. With a vertically incident signal from the satellite, a strongly focused radiation field is observed at the reception antenna array, located at 2 *cm* from the metasurface. Even with obliquely incident signals (*e.g.*, 20°), the radiation field is shifted but can still be reliably received by the antenna array. By employing our proposed metasurface with optimized downlink phase map compensation, our system can effectively focus incoming signals from a broad range of incident angles.

Multiple satellites receiving support: Our metasurface can also support multi-satellite downlink communication. As satellites within the field of view transmit signals of varying frequencies towards the metasurface, it can independently focus incoming signals of different frequencies and enhance the RSS of each satellite transmission. Subsequently, the ground station can effectively distinguish the enhanced signals in the frequency domain and successfully decode the transmitted data from each individual satellite. Hence, our system inherently supports the reception from multiple satellites simultaneously.

4 EVALUATION

In this section, we first introduce our prototype implementation and experimental testbed setup. We then describe our evaluation methodology and performance results.

4.1 Manufactured prototype

The fabricated prototype of the PMSat, depicted in Fig. 11(a), consists of a passive metasurface and two multiple antenna arrays for uplink and downlink. The antenna arrays are separated from the metasurface by a 3D-printed bracket, with a distance of 2 *cm*, aligning the centers of the metasurface and the uplink antenna array.

Dual-band metasurface: The metasurface is fabricated using standard photolithographic techniques on a F4BM220 (2.2

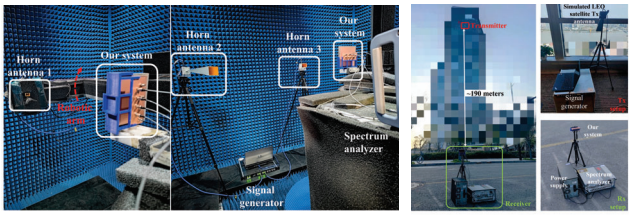

(a) Anechoic chamber (b) Outdoor environment

Figure 13: Experimental testbeds setup

permittivity, 0.001 loss tangent, and 0.254*mm* thickness) sheet. The metasurface has 21 × 21 and 22 × 22 elements for the uplink and downlink, respectively. The phase profiles for the uplink and downlink are obtained through optimization models described in Sec. 3.2 and 3.3, respectively, and the detailed phase distributions are shown in Fig. 12. The overall size of our proposed full four-layer metasurface is 12.66*cm* × 12.66*cm* × 1.17*cm*, with a weight of 80.25*g*.

Antenna arrays: We design two microstrip patch antenna arrays. These arrays were fabricated on a 0.381 *mm* thick F4BM220 substrate, as depicted in Fig. 11(c). For the uplink TX antennas, we design a 1 × 4 linear array with 2 *cm* (*i.e.*, 2 wavelength) spacing. Each TX antenna consists of 2 × 2 square patch sub-antennas. Similarly, for the downlink RX antennas, we also design a 1 × 4 linear array with 3 *cm* (*i.e.*, 2 wavelength) spacing. RX antenna consists of 2 × 2 square patch sub-antennas with the same feeding port.

4.2 Experimental testbed setup

Two experimental testbeds are established to evaluate the performance of our proposed PMSat. The first is deployed in a microwave anechoic chamber to mimic the plane-wave signals transmitted by LEO satellites, while minimizing the multipath effects. The second is an outdoor open space (*i.e.*, a skyscraper) used to mimic LEO antenna operations at an altitude of 190 meters.

To test the uplink, we utilize a phase-coherent four-channel signal generator, AnaPico APMS40G-ULN [24], connected to the uplink TX antenna array. An off-the-shelf BJ320 (WR-28) linearly polarized horn antenna serves as the receiver (*i.e.*,

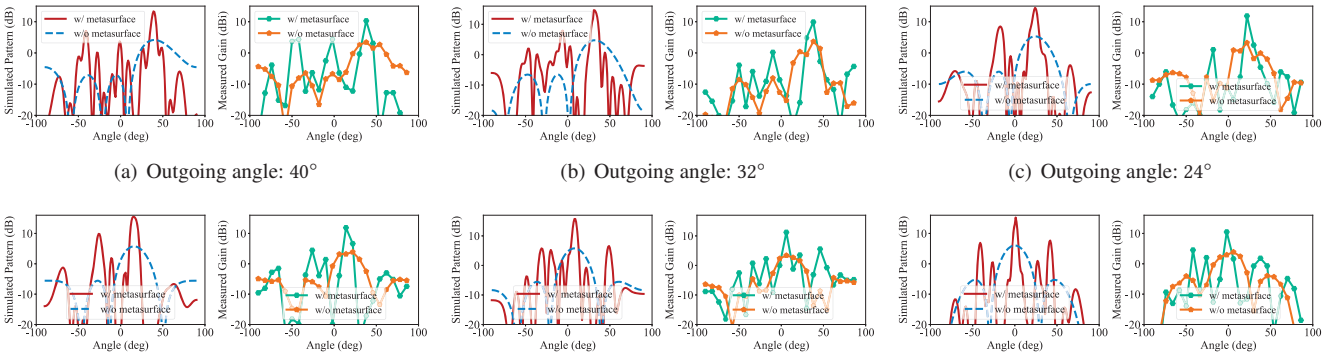

(a) Outgoing angle: 40° (b) Outgoing angle: 32° (c) Outgoing angle: 24°

(d) Outgoing angle: 16° (e) Outgoing angle: 8° (f) Outgoing angle: 0°

Figure 14: Simulated and measured beam patterns for outgoing directions of 1×4 antennas with and without 21×21 metasurface. Left figure of each subplot is theoretical analysis result and right is anechnoic chamber experiment result

a simulated satellite RX antenna), which is connected to a spectrum analyzer to obtain the RSS. We use the following equation to calculate the far-field conditions: $\frac{2D_tD_r}{\lambda}$, where D_t and D_r are the diameters of the Tx and Rx antennas, and λ is the wavelength. By using the metasurface as TX and a horn antenna as RX, we can calculate that the far-field condition to be 0.76 m for the uplink. In the anechoic chamber testbed, we fix the RX antenna on a robotic arm at a distance of 1 m from our system to satisfy the far-field condition and the details are shown in the left side of Fig. 13(a). We control the robotic arm to perform a $-90° \sim 90°$ rotation in an elevation-cut plane (when the azimuth angle is 0°) to measure the steering beam pattern precisely. In the open outdoor space, we deploy our ground station on the ground, and deploy the other side's antennas on the 43rd floor of an office building at an altitude of 190 m above the ground. We test the performance of our system in three specific locations, and one of which is illustrated in Fig. 13(b).

To test the downlink, we use two off-the-shelf BJ220 (WR-42) linearly polarized horn antennas, whose frequencies are $17.6 \sim 26.7$ GHz, to emulate antennas on one or two LEO satellites. We feed signals to TX antennas with AnaPico APMS40G-ULN, and measure the received signal strength from each antenna in our system by the spectrum analyzer in turn. The far-field condition for the downlink is 1.69 m. In the anechoic chamber testbed, we position the horn antennas 2 m away from our system to satisfy the far-field condition, as shown in the right of Fig. 13(a). The setup for the downlink in the open space testbed is similar to that for the uplink.

4.3 Evaluation Methodology

The proposed PMSat is evaluated extensively in three ways: theoretical analysis, numerical EM propagation simulation, and real-world experiment. Theoretical simulation supports efficient analysis under diverse conditions from a high level perspective. Ansys HFSS utilizes a numerical technique, called Finite Element Method (FEM), and provides detailed simulations of the EM propagation of the metasurface and phased array to validate the theoretical simulation. The two testbed experiments mentioned above serve as a final validation by testing the prototype system in real-world environments.

4.3.1 Uplink Performance. **Comparison of beam steering with phased arrays:** We first compare the beam steering performance of our proposed system and the phased array alone by using the corresponding codeword for each system to measure beam patterns from 0° to 40° at $30GHz$. As shown in Fig. 14, the measured beam patterns of our PMSat closely match the theoretical simulation results. Moreover, our proposed system generates sharper beams in the desired directions than the phased array. This is evident from both simulation and real-world testbed measurement. We also observe that the signal strength of the beam is $6.60 \sim 8.68$ dBi higher in the desired direction than the phased array alone.

Next we examine the spatial divergence of the beams generated by our system. As shown in Fig. 8(b) and 8(a), multiple phase arrays would typically be deployed in a 3D space to achieve the intensity of the EM field measurements. Instead, we evaluate the divergence of our system by measuring the beamwidth and gain. The results show that our system achieve an average of 10.7° and 13.61 dBi gain when steering outgoing signals across ±40°, while the phased array only has an an average beamwidth of 31.2° and gain of $5.29dBi$. The above results show that our system has less beam divergence during the propagation than the 1× phased array.

Impact of different frequencies: We investigate the performance change of our system as the operation frequency varies. We measure the signal strength gains along various outgoing directions in the anechoic chamber. As shown in Fig. 15, the gain ranges from 9.21 dBi to 11.59 dBi between −40° and 40° at 30 GHz. The steering performance in terms of signal strength at 29 GHz − 29.9 GHz are similar to the gains at 30 GHz. However, when the frequency deviates too much

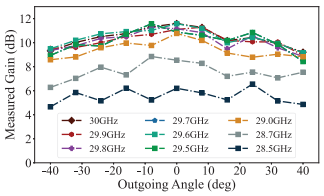

Figure 15: Measured performance at different frequencies in the anechoic chamber

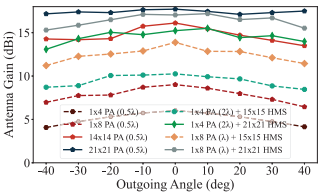

Figure 16: Simulated performance of different size of PA and metasurface

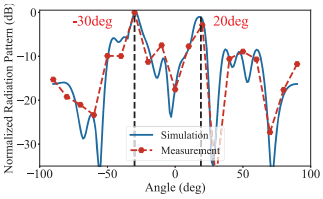

Figure 17: Experiment results of supporting multiple outgoing directions

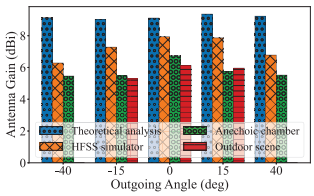

Figure 18: Comparison of steering performance using different evaluation methods

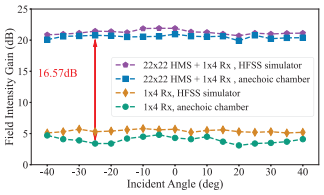

Figure 19: Focusing performance with and without 22×22 metasurface

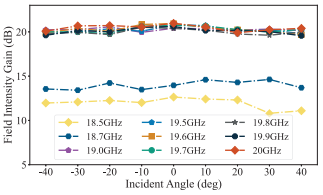

Figure 20: Simulated focusing performance under different frequencies

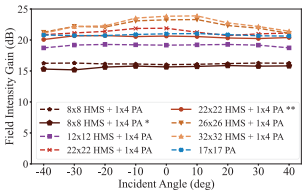

Figure 21: Simulated focusing performance of different sizes of PA and metasurface

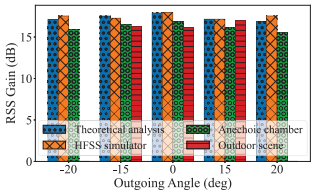

Figure 22: Comparison of focusing performance in different evaluation manners

from 30 GHz, the gain decreases noticeably. For example, at 28.7GHz, the gains decrease to a range of $6.27-9.17$ dBi; and at 28.5 GHz, the gains decrease to a range of $4.66-6.75$ dBi. Therefore, the above results show that our metasurface unit design can indeed support a bandwidth of 2 GHz (± 1 GHz difference from the center frequency), which is sufficient for LEO satellite communication scenarios.

Impact of phased array size and metasurface size: We study the performance differences of our system as we vary the metasurface and phased array sizes. We also compare our system with the traditional massive phased array system of different sizes. From Fig. 16, we observe (i) increasing the phased array size and metasurface elements in our system design indeed improves the steering performance and directionality; (ii) our system with a 1×4 phased array and a 21×21 metasurface out-performs 1×21 linear phased array because our system uses a 2D metasurface to focus the energy in two dimensions. It is also comparable to a 14×14 phased array. When our system is equipped with a 1×8 phased array and a 21×21 metasurface, it can achieve almost the same steering performance as a 21×21 massive phased array, which is the upper bound of the 21×21 metasurface.

Steering towards multiple satellites: Fig. 17 shows the performance when our system steers the outgoing beam towards two satellites at $-30°$ and $20°$ simultaneously. The results indicate that even with only 1×4 phased array, PMSat can steer the outgoing signals to multiple desired angles simultaneously. However, it is important to note that there are inevitable sidelobes at other undesirable angles. Nevertheless, the RSS of these side lobes is -8 dB lower than the main lobes, which can easily support reliable wireless communication.

Outdoor experimental results: We further evaluate our system outdoors. Specifically, we test the performance three times by changing the position of our ground station while fixing the satellite antenna at the 43rd floor to test the steering directions of $-15°$, $0°$, and $15°$, respectively. We adjust the receiving angle of the satellite antenna to ensure that it receives signals from our system. Experimental results in Fig. 18 indicate that our outdoor experiments achieve similar performance to our anechoic chamber experiments. We also include results from theoretical analysis, HFSS, and anechoic chamber for $\pm40°$ and observe similar performance across them. The reception device on the ground needs to be moved to the road for the outdoor experiments of a wide angle. Considering the safety, we skip our outdoor experiment at $\pm40°$.

4.3.2 Downlink Performance. **Comparison of focusing performance with phased array:** The phased array antennas can also increase RSS. We compare the performance of our system with that of the phased array on the received signal. Fig. 19 compares the field intensity with a single receiving antenna for the downlink when the incident angle varies from $-40°$ to $40°$. We make the following observations. First, the results from the anechoic chamber align pretty well with that of the simulation across a wide of incident angles. Second, adding our metasurface significantly increases RSS, as we would expect. We observe an average of 16.57 dB improvement over a 1×4 phased array. This is because the metasurface is equivalent to a large-aperture antenna, which can focus EM signals from a bigger area onto the receiving antenna array, yielding a considerable RSS gain.

Impact of frequency: Fig. 20 shows the field intensity gain for the downlink across different incident angles as the operation frequency changes. The results show that our metasurface can effectively focus the incoming EM waves to enhance RSS from $-40° \sim 40°$ incident angles across a wide band in the downlink. The field intensity gain remains high at around

20.4 dB when the frequency spans between 19 $GHz \sim 20\ GHz$. However, the average field intensity gain decreases to 14.3dB at 18.7 GHz and to 12.3dB at 18.5GHz. A 1 GHz bandwidth is sufficient to meet the downlink requirements. Meanwhile, the metasurface also helps prevent amplification of noise or interference signals close to the operating frequency.

Impact of phased array size and metasurface size: We compare our system performance with a massive phased array as we vary the numbers of metasurface elements with a 1×4 antenna array. From Fig 21, we observe that all curves from Matlab simulation match the results derived from HFSS simulation and anechoic chamber experiments. Furthermore, we can clearly observe that the larger the metasurface, the higher the gain. This is well aligned with our expectation. Specifically, 32×32, 26×26, 22×22, 16×16, 12×12, and 8×8 achieve 23.54dB, 23.17dB, 21.86dB, 21.13dB, 19.22dB, and 16.24dB, respectively. In addition, the gain remains nearly unchanged when the incident angle shifts from $-40°$ to $40°$ for all metasurface sizes except the two largest sizes: 32×32 and 26×26, which experience slight drops. Nevertheless, the beam focusing effect is still preserved even in the presence of slight drops. For example, a 22×22 metasurface combined with 1×4 multiple antennas achieves the same focusing effect as the 17×17 massive phased array.

Outdoor experimental results: We also conduct the outdoor experiments to validate the effectiveness of our system. We test the focusing performance at three incident directions: $-15°$, $0°$, and $15°$. Experimental results in Fig. 18 show that our system achieves almost the same focusing performance in the outdoor scenario as in the anechoic chamber experiments.

4.3.3 Comparison with Related Works. Recent literature employs passive metasurfaces to enhance the performance of phased array antennas and reduce the number of phase shifters [22, 37]. In this section, we compare with two closest work. [22] uses a metasurface with a gradient phase profile to expand steering angle range from $[-30°, 30°]$ to $[-40°, 40°]$, but does not optimize RSS (*i.e.*, the gain of the main lobe). Unlike [22], our work jointly optimizes the metasurface and phased array to achieve dynamic beam steering. We can achieve a $\pm 60°$ steering range using a 1×8 PA and 21×21 metasurface at 30 GHz, as shown in Fig.23. Our simulation results show that our system can achieve steering performance with an average beamwidth of $10.3°$ and 9.1 dB gain across $\pm 60°$ range. Our system can achieve an average beamwidth of $9.2°$ and 5.7 dB gain for $\pm 80°$. [37] uses traditional phase compensation to generate a highly directional beam using five phased-array antennas targeting five specific angles. Our approach uses a single optimized phased array and metasurface design to enable beam steering for any angle within a given range (*e.g.*, from $-60°$ to $60°$).

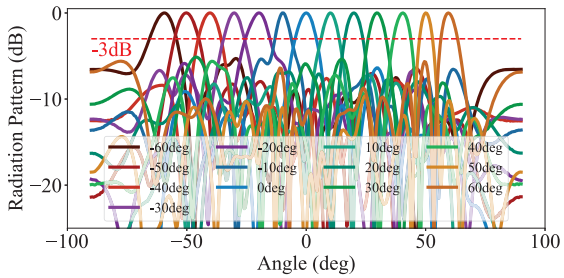

Figure 23: Our systems can support dynamic steering over a wider angular range from $-60°$ to $60°$

4.3.4 Cost Comparison. Our PMSat prototype features a metasurface PCB board (\$30 [34]), a microstrip patch antenna array with 1×4 reception antennas and 1×4 transmission antennas (\$10), and only four digital phase shifters [18] ($\simeq$ \$50) for the uplink antenna array. The total cost is around \$90. In comparison, a phased array approach requires 14×14 antennas in order to achieve comparable steering performance (*e.g.*, beamwidth and gain) to our system in the uplink, and requires 17×17 antennas to achieve comparable focusing performance in the downlink. The massive phased array transceiver requires up to 289 patch antennas as well as 289 digital phase shifters (*i.e.*, around 40 times of our cost). This estimate is conservative. In practice, there are more cable costs and computational resources costs incurred in phased array only scheme. Therefore, we believe our system is a cost-effective solution for LEO satellite communication ground stations.

5 CONCLUSION

In this paper, we present a novel ground station design with a phased array-coupled passive metasurface for LEO satellite communication. We design a meta-atom structure that can achieve high transmittance and full phase shift modulation capability for a variety of incident angles. We further jointly optimize the phased array antenna and the phase profile of the metasurface to support dynamic beam steering for the uplink and realize high gained RSS enhancement for the downlink. We develop a PMSat system prototype and it yields 8.32 dB and 16.57 dB strength enhancement over the same sized phased array in the uplink and downlink, respectively. Moving forward, we are interested in conducting field tests using real satellite signals. Moreover, while our current focus is on LEO satellite communication, our joint optimization of the metasurface and phased array could also be applied to other wireless networks, such as extending mmWave coverage.

ACKNOWLEDGMENTS

We are grateful to anonymous reviewers for their constructive comments. We also thank Ruichun Ma for his enlightening discussions.

REFERENCES

[1] I. Ali, N. Al-Dhahir, and J. E. Hershey. Doppler characterization for leo satellites. *IEEE transactions on communications*, 46(3):309–313, 1998.

[2] Ansys. Ansys hfss best-in-class 3d high frequency electromagnetic simulation software. https://www.ansys.com/products/electronics/ansys-hfss, 2022.

[3] V. Arun and H. Balakrishnan. {RFocus}: Beamforming using thousands of passive antennas. In *17th USENIX symposium on networked systems design and implementation (NSDI 20)*, pages 1047–1061, 2020.

[4] A. O. Bah, P.-Y. Qin, R. W. Ziolkowski, Q. Cheng, and Y. J. Guo. Realization of an ultra-thin metasurface to facilitate wide bandwidth, wide angle beam scanning. *Scientific reports*, 8(1):1–11, 2018.

[5] J. Bergstra, R. Bardenet, Y. Bengio, and B. Kégl. Algorithms for hyper-parameter optimization. *Advances in neural information processing systems*, 24, 2011.

[6] S. Cakaj. The parameters comparison of the "starlink" leo satellites constellation for different orbital shells. https://www.frontiersin.org/articles/10.3389/frcmn.2021.643095/full, 2023.

[7] L. Chen, W. Hu, K. Jamieson, X. Chen, D. Fang, and J. Gummeson. Pushing the physical limits of {IoT} devices with programmable metasurfaces. In *18th USENIX Symposium on Networked Systems Design and Implementation (NSDI 21)*, pages 425–438, 2021.

[8] M. Chen, M. Kim, A. M. Wong, and G. V. Eleftheriades. Huygens' metasurfaces from microwaves to optics: a review. *Nanophotonics*, 7(6):1207–1231, 2018.

[9] K. W. Cho, Y. Ghasempour, and K. Jamieson. Towards dual-band reconfigurable metamaterial surfaces for satellite networking. *arXiv preprint arXiv:2206.14939*, 2022.

[10] K. W. Cho, M. H. Mazaheri, J. Gummeson, O. Abari, and K. Jamieson. mmwall: A reconfigurable metamaterial surface for mmwave networks. In *Proceedings of the 22nd International Workshop on Mobile Computing Systems and Applications*, pages 119–125, 2021.

[11] F. C. Commission. Application for authority to deploy and operate a ka-band non-geostationary satellite orbit system. https://docs.fcc.gov/public/attachments/FCC-20-102A1.pdf, 2022.

[12] I. Del Portillo, B. G. Cameron, and E. F. Crawley. A technical comparison of three low earth orbit satellite constellation systems to provide global broadband. *Acta astronautica*, 159:123–135, 2019.

[13] B. Feng, L. Li, Q. Zeng, and K. L. Chung. A wideband antenna using metasurface for the 2g/3g/lte/5g communications. *Microwave and Optical Technology Letters*, 60(10):2482–2487, 2018.

[14] H. Hao, X. Ran, Y. Tang, S. Zheng, and W. Ruan. A single-layer focusing metasurface based on induced magnetism. *Prog. Electromagn. Res*, 172:77–88, 2021.

[15] S. E. Hosseininejad, K. Rouhi, M. Neshat, A. Cabellos-Aparicio, S. Abadal, and E. Alarcón. Digital metasurface based on graphene: An application to beam steering in terahertz plasmonic antennas. *IEEE Transactions on Nanotechnology*, 18:734–746, 2019.

[16] J. Hu, H. Zhang, B. Di, L. Li, K. Bian, L. Song, Y. Li, Z. Han, and H. V. Poor. Reconfigurable intelligent surface based rf sensing: Design, optimization, and implementation. *IEEE Journal on Selected Areas in Communications*, 38(11):2700–2716, 2020.

[17] C. Huang, C. Zhang, J. Yang, B. Sun, B. Zhao, and X. Luo. Reconfigurable metasurface for multifunctional control of electromagnetic waves. *Advanced Optical Materials*, 5(22):1700485, 2017.

[18] R. E. A. Inc. Rf and wireless rf transceiver ics ra81f5268stgbxbc0. https://www.digikey.com/en/products/detail/RA81F5268STGBX%2523BC0/800-RA81F5268STGBX%2523BC0-ND/18160251, 2023.

[19] W. Khawaja, O. Ozdemir, Y. Yapici, F. Erden, and I. Guvenc. Coverage enhancement for nlos mmwave links using passive reflectors. *IEEE Open Journal of the communications Society*, 1:263–281, 2020.

[20] D. P. Kingma and J. Ba. Adam: A method for stochastic optimization. *arXiv preprint arXiv:1412.6980*, 2014.

[21] E. B. Lima, S. A. Matos, J. R. Costa, C. A. Fernandes, and N. J. Fonseca. Circular polarization wide-angle beam steering at ka-band by in-plane translation of a plate lens antenna. *IEEE Transactions on Antennas and Propagation*, 63(12):5443–5455, 2015.

[22] Y.-H. Lv, X. Ding, B.-Z. Wang, and D. E. Anagnostou. Scanning range expansion of planar phased arrays using metasurfaces. *IEEE Transactions on Antennas and Propagation*, 68(3):1402–1410, 2020.

[23] J. G. McWhirter, P. D. Baxter, T. Cooper, S. Redif, and J. Foster. An evd algorithm for para-hermitian polynomial matrices. *IEEE Transactions on Signal Processing*, 55(5):2158–2169, 2007.

[24] A. of Switzerland. Apms-uln models - multi-channel signal generator up to 40 ghz. https://www.anapico.com/products/rf-signal-generators/multi-channel-analog-and-digital-signal-generator/apms-models-multi-channel-signal-generators-up-to-40-ghz/, 2022.

[25] Pasternack. 8-bit digital phase shifters offer 360 degrees of highly accurate. https://www.pasternack.com/pages/rf-microwave-and-millimeter-wave-products/digital-phase-shifters.html, 2023.

[26] Z. Peng, L. Li, M. Wang, Z. Zhang, Q. Liu, Y. Liu, and R. Liu. An effective coverage scheme with passive-reflectors for urban millimeter-wave communication. *IEEE Antennas and Wireless Propagation Letters*, 15:398–401, 2015.

[27] J. G. Proakis and M. Salehi. *Digital communications*, volume 4. McGraw-hill New York, 2001.

[28] K. Qian and X. Zhang. Millimirror: 3d printed reflecting surface for millimeter-wave coverage expansion. In *Proceedings of the ACM Annual International Conference on Mobile Computing and Networking (MobiCom)*, 2022.

[29] SatNOGS. Satnogs. https://satnogs.org/, 2022.

[30] N. T. R. Server. The recent large reduction in space launch cost. https://ntrs.nasa.gov/citations/20200001093, 2018.

[31] V. Singh, A. Prabhakara, D. Zhang, O. Yağan, and S. Kumar. A community-driven approach to democratize access to satellite ground stations. In *Proceedings of the 27th Annual International Conference on Mobile Computing and Networking*, 2021.

[32] X. Tan, Z. Sun, D. Koutsonikolas, and J. M. Jornet. Enabling indoor mobile millimeter-wave networks based on smart reflect-arrays. In *IEEE INFOCOM 2018-IEEE Conference on Computer Communications*, pages 270–278. IEEE, 2018.

[33] W. Tang, J. Y. Dai, M. Z. Chen, K.-K. Wong, X. Li, X. Zhao, S. Jin, Q. Cheng, and T. J. Cui. Mimo transmission through reconfigurable intelligent surface: System design, analysis, and implementation. *IEEE journal on selected areas in communications*, 38(11):2683–2699, 2020.

[34] A. Taobao. Rogers 5880 supply ro3003 and tly-5 rogers proofing mass production in-stock high frequency plates. https://item.taobao.com/item.htm?spm=a230r.1.14.18.6fd63cbe4Lj6BA&id=669858288043&ns=1&abbucket=16#detail, 2023.

[35] A. Wainscott-Sargent. Leo advances on the ground: Antenna and gateway technology will play a crucial role as the industry moves into the leo era. https://interactive.satellitetoday.com/leo-advances-on-the-ground/, 2023.

[36] Q. Wang, E. T. Rogers, B. Gholipour, C.-M. Wang, G. Yuan, J. Teng, and N. I. Zheludev. Optically reconfigurable metasurfaces and photonic devices based on phase change materials. *Nature photonics*, 10(1):60–65, 2016.

[37] R. Xu and Z. N. Chen. A compact beamsteering metasurface lens array antenna with low-cost phased array. *IEEE Transactions on Antennas and Propagation*, 69(4):1992–2002, 2020.

[38] R. I. Zelaya, W. Sussman, J. Gummeson, K. Jamieson, and W. Hu. Lava: fine-grained 3d indoor wireless coverage for small iot devices. In *Proceedings of the 2021 ACM SIGCOMM 2021 Conference*, pages

123–136, 2021.

[39] L. Zhang, J. Guo, and T. Ding. Ultrathin dual-mode vortex beam generator based on anisotropic coding metasurface. *Scientific Reports*, 11(1):1–8, 2021.

[40] X. Zhou, Z. Zhang, Y. Zhu, Y. Li, S. Kumar, A. Vahdat, B. Y. Zhao, and H. Zheng. Mirror mirror on the ceiling: Flexible wireless links for data centers. *ACM SIGCOMM Computer Communication Review*, 42(4):443–454, 2012.